Obrabotka metallov (tekhnologiya, oborudovanie, instrumenty) = Metal Working and Material Science. 2025 vol. 27 no. 4 pp. 221–238
ISSN: 1994-6309 (print) / 2541-819X (online)
DOI: 10.17212/1994-6309-2025-27.4-221-238

NSTU NETI

Obrabotka metallov - Metal Working and Material Science

Journal homepage: http://journals.nstu.ru/obrabotka_metallov

Study of tribological properties of silicon bronze in different structural states

Andrey Filippov [a, *], *Nikolay Shamarin* [b], *Sergei Tarasov* [c]

Institute of Strength Physics and Materials Sciences SB RAS, 2/4 per. Academicheskii, Tomsk, 634055, Russian Federation

[a] https://orcid.org/0000-0003-0487-8382, avf@ispms.ru; [b] https://orcid.org/0000-0002-4649-6465, shnn@ispms.ru;
[c] https://orcid.org/0000-0003-0702-7639, tsy@ispms.ru

ARTICLE INFO

Article history:
Received: 13 August 2025
Revised: 03 September 2025
Accepted: 09 September 2025
Available online: 15 December 2025

Keywords:
Electron beam
Silicon bronze
Structure
Vibration
Acoustic emission
Mechanical properties
Severe plastic deformation
Sliding friction

Funding
This research was funded by Russian Science Foundation project No. 24-29-00259, https://rscf.ru/project/24-29-00259/.

ABSTRACT

Introduction. Silicon bronzes are widely used in critical friction units due to their combination of corrosion resistance, machinability, electrical conductivity, and satisfactory mechanical properties. Electron beam additive manufacturing (*EBAM*) is promising for the production of complex parts, but it forms a large columnar grain structure, leading to anisotropy of properties and limiting their practical application. Methods of severe plastic deformation (*SPD*), such as multi-axis forging and rolling, are effective for refining the structure, eliminating anisotropy, and increasing strength. However, their effect on the overall properties of silicon bronzes has not been sufficiently studied. **Purpose of the work.** The purpose of this study is a comparative analysis of the effect of the structural state of silicon bronze on its mechanical characteristics and tribological properties under dry sliding friction. **Research methods.** Samples in five structural states were obtained by electron-beam additive manufacturing (1), hot rolling (2), multi-axis forging (3), rolling at room temperature (4), and low-temperature annealing after rolling (5). The structure of the samples was investigated by optical metallography and transmission electron microscopy. Mechanical tests were carried out by tensile testing of double-sided dog-bone samples and Vickers microhardness testing. Tribological tests for dry sliding friction against 52100 steel were carried out with a constant load and speed. During friction, the friction coefficient (*FC*), vibrations in the normal and tangential directions, and acoustic emission (*AE*) were recorded. A detailed analysis of the surface and subsurface layer of friction tracks was performed using confocal laser scanning microscopy, as well as scanning electron microscopy with energy-dispersive X-ray spectroscopy (*EDS*). **Results and discussion.** The microstructure of the samples after *EBAM* exhibits large columnar grains, while after hot rolling it shows large equiaxed grains with twins. Multi-axial forging results in the formation of subgrains (lamellae) (<100 nm) with a high dislocation density. Rolling leads to further refinement of the original grains and the formation of elongated submicron grains. Low-temperature annealing forms more equiaxed submicron grains (100–200 nm) with a reduced dislocation density and high-angle boundaries. Samples with a coarse-grained structure have low strength and hardness. After *SPD*, the strength and hardness increase significantly, and the relative elongation decreases compared to the original material. Low-temperature annealing provides maximum strength with partial restoration of ductility and a decrease in hardness. The smallest and most stable friction coefficient, as well as minimum vibration amplitudes (especially in the tangential direction), were recorded for samples after *SPD*. The greatest wear occurred for the sample in the as-received condition (hot rolling). *SPD* reduces wear by 2.1–2.2 times compared to the hot-rolled and *EBAM* samples. Low-temperature annealing increases wear by 10% relative to the sample after rolling. The predominant wear mechanisms were determined to be: mixed (adhesive-oxidative) for bronze after *EBAM*; adhesive for hot rolled; and oxidative for samples after *SPD*. Based on metallographic studies, it was found that the depth of subsurface deformation is maximum for coarse-grained samples (145–155 μm) and decreases by 3.3–4.7 times after *SPD*. ***Conclusion***. A comprehensive study has revealed a decisive influence of the structural state of 96% *Cu*-3% *Si*-1% *Mn* bronze on its key properties. The use of *SPD* methods (multi-axial forging and rolling) has proven to be highly effective in dramatically improving the mechanical and tribological properties of silicon bronze, regardless of the original production method (hot-rolled steel or electron beam additive manufacturing).

For citation: Filippov A.V., Shamarin N.N., Tarasov S.Yu. Study of tribological properties of silicon bronze in different structural states. *Obrabotka metallov (tekhnologiya, oborudovanie, instrumenty) = Metal Working and Material Science*, 2025, vol. 27, no. 4, pp. 221–238. DOI: 10.17212/1994-6309-2025-27.4-221-238. (In Russian).

Introduction

Silicon bronzes, a class of copper-based alloys containing 1–4 wt.% silicon, are widely used in various industries due to their unique combination of high corrosion resistance, good machinability, excellent electrical and thermal conductivity, and satisfactory mechanical and antifriction properties. These alloys are commonly employed in the manufacture of plain bearings, bushings, gears, valves for aggressive media, and electrical components [1]. Conventionally, silicon bronze products are produced via casting followed by thermomechanical processing (e.g., rolling, forging, pressing) or through powder metallurgy routes.

*** Corresponding author**
Filippov Andrey V., Ph.D. (Engineering), Head of Laboratory
Institute of Strength Physics and Materials Sciences SB RAS,
2/4 per. Academicheskii,
634055, Tomsk, Russian Federation
Tel.: +7 999 178-13-40, **e-mail:** avf@ispms.ru

Binary *Cu-Si* alloys with silicon contents below 5 wt.% consist of a single-phase face-centered cubic (*FCC*) α-*Cu* solid solution [2]. The addition of manganese refines the dendritic grain structure without altering the phase composition, as demonstrated in cast *Cu-3Si* alloy [3, 4]. This grain refinement is accompanied by improvements in ductility, tensile strength, and hardness. It has been established that significant alterations in solid-phase reactions can be achieved by modifying the processing scale, temperature, or initial microstructure [5]. While heat treatment can influence the microstructure and phase composition of silicon bronzes [6], the low-silicon α-*Cu* solid solution is not susceptible to phase transformations [7].

Recently, wire and electron beam additive manufacturing (*WEBAM*) has garnered significant interest for fabricating silicon bronze components. This highly productive technique enables the creation of complex, custom geometries with minimal machining allowances. However, an inherent characteristic of additively manufactured metals, including those produced by *WEBAM*, is epitaxial solidification, which leads to the formation of coarse columnar grains [8]. This microstructure results in pronounced anisotropy of mechanical properties and can adversely affect tribological characteristics, thereby limiting the application of these materials in highly-loaded friction units that require isotropic behavior.

Severe plastic deformation (*SPD*) techniques, such as equal-channel angular pressing (*ECAP*), multi-axis forging, and rolling, are highly effective for mitigating these drawbacks and enhancing the mechanical properties of alloys, including silicon bronze. *SPD* methods can significantly refine the coarse, columnar grain structure, transforming it into an ultrafine-grained (*UFG*) or nanocrystalline (*NC*) state with equiaxed grains, thereby eliminating anisotropy. The resultant grain boundary strengthening leads to substantial improvements in strength and hardness. A subsequent short-term, low-temperature annealing step is often employed to partially relieve internal stresses and improve ductility without sacrificing a significant portion of the strength gained from strain hardening. This balance is critical for tribological applications requiring a combination of high strength and wear resistance.

Previous research has demonstrated the efficacy of *SPD*; for instance, hydrostatic extrusion of *C65500* bronze (an analog of *96% Cu-3% Si-1% Mn*) increased its tensile strength and yield strength by 45% and 130%, respectively, compared to the commercial counterpart [8]. Similarly, the transformation of a columnar grain structure into an equiaxed, twinned one was achieved in a *96% Cu-3% Si-1% Mn* alloy through drawing followed by softening annealing [9]. These findings confirm that *SPD* is a viable strategy for microstructural refinement and property enhancement in silicon bronzes. However, a review of the literature indicates that the potential of specific *SPD* methods, particularly multi-axis forging and rolling, for processing silicon bronzes remains insufficiently explored.

Therefore, ***the purpose of this work*** is to conduct a comparative study of the mechanical and tribological properties of a silicon bronze in different structural states. The following ***tasks*** were defined to achieve this purpose:

1. Perform microstructural characterization.
2. Conduct mechanical testing.
3. Perform tribological tests under dry sliding friction conditions.
4. Analyze the friction surface and subsurface deformation layers after sliding.

Methods

Silicon bronze samples were produced using a wire-feed electron beam additive manufacturing (*WEBAM*) machine to fabricate layer-by-layer deposits from a *96% Cu-3% Si-1% Mn* wire onto steel substrates. The printing parameters for these block-shaped samples were implemented in accordance with modes detailed in reference [11]. These samples correspond to the first structural state, characterized by large columnar grains, and are designated herein as Sample 1.

The second structural state comprises a material with large equiaxed grains and annealing twins, characteristic of the microstructure found in commercial hot-rolled bar stock. Samples in this condition are designated as Sample 2.

The third structural state features a subgrain structure consisting of submicron lamellae, formed by subjecting the *WEBAM*-fabricated samples (Sample 1) to severe plastic deformation via multi-axial forging

at room temperature. The process was conducted at a constant crosshead speed of 10 mm/s until a degree of deformation of ε = 0.5 was achieved along each of the three geometric axes of the sample. These samples are designated as Sample 3.

The fourth structural state is a material with submicron grains, produced by further processing Sample 3 through multiple passes of room-temperature rolling to a total strain of ε = 0.75. These samples are designated as Sample 4.

The fifth structural state comprises a material with near-equiaxed submicron grains, produced by subjecting Sample 4 to a low-temperature annealing at 200 °C for 30 minutes. The heat treatment was conducted in a laboratory muffle furnace, followed by rapid quenching in a large volume of water. These samples are designated as Sample 5.

The mechanical properties of the samples were determined by tensile testing standard double-sided blade specimens on a *Testsystems UTS-110M* universal testing machine at a crosshead speed of 1 mm/min. Vickers microhardness was measured using a *Tochline-TBM* hardness tester by indenting the samples with a diamond pyramid under a load of 100 N (HV10).

Metallographic analysis of samples in the rolled and as-printed conditions was performed using an *Olympus LEXT 4100* laser scanning confocal microscope. The fine microstructure of samples after severe plastic deformation was characterized by transmission electron microscopy (*TEM*) using a *JEOL JEM-2100* microscope.

For tribological testing, plate-shaped samples were prepared for sliding contact against 6 mm diameter balls made of *ShKh15* (*AISI 52100* equivalent) bearing steel. Tests were conducted under dry sliding conditions at a velocity of 100 mm/s under a normal load of 20 N. During friction, acoustic emission signals and vibration amplitudes were recorded. Vibration accelerations were measured in both the normal (parallel to the applied load) and tangential (parallel to the friction force) directions. The morphology of the resulting wear tracks was examined using scanning electron microscopy (*Thermo Fisher Scientific Apreo S LoVac*) and laser scanning microscopy (*Olympus LEXT 4100*).

Results and Discussion

Wire and electron beam additive manufacturing (Sample 1) results in the formation of a large columnar grain structure (Fig. 1, *a*). The grain width ranges from 150 to 600 μm, with lengths often significantly exceeding 1 mm. This microstructure results from directional solidification under the pronounced thermal gradient of the melt pool during layer-by-layer deposition. Samples in the as-received hot-rolled condition (Sample 2) exhibit a microstructure of nearly equiaxed grains with annealing twins (Fig. 1, *b*), with grain size ranging from 200 to 500 μm.

Multi-axial forging (Sample 3) produces a highly deformed substructure characterized by significant azimuthal misorientation, arising from strain-induced grain subdivision and refinement. The subgrain structure consists of curved, submicron lamellae with thicknesses below 100 nm, formed during non-uniform deformation in the forging process. This state is also characterized by a high dislocation density. Subsequent rolling (Sample 4) further refines the structure into elongated submicron grains (Fig. 1, *d*). The selected area electron diffraction (*SAED*) pattern exhibits a substantial increase in azimuthal misorientation, with reflections degenerating into nearly continuous rings, indicating extreme grain refinement. This grain formation likely results from recovery and dynamic recrystallization processes during severe plastic deformation [12].

Low-temperature annealing (Sample 5) after rolling reduces the dislocation density and promotes the formation of nearly equiaxed submicron grains, ranging from 100 to 200 nm in size (Fig. 1, *e*).

Tensile testing revealed that the different structural states exhibit distinct combinations of strength and ductility (Fig. 2, *a–c*). The *WEBAM*-fabricated and as-received hot-rolled samples (Sample 1 and Sample 2) demonstrated the lowest strength but highest ductility. Their ultimate tensile strength (*UTS*) was nearly identical, at 340–346 MPa. However, their yield strength differed significantly, by approximately a factor of two, with the *WEBAM* sample exhibiting a characteristically low yield stress, a known trait of structures formed by electron beam printing [13].

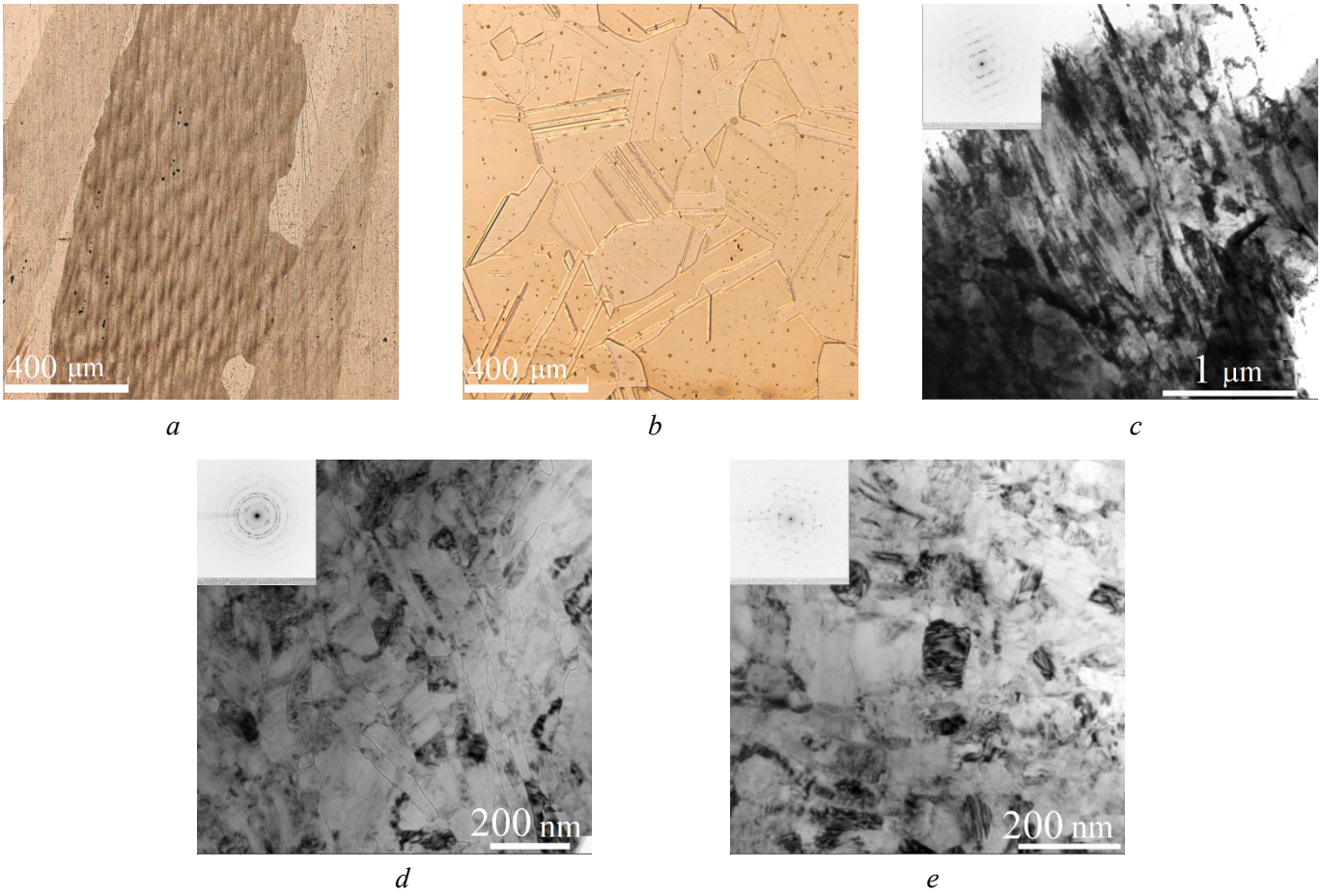

a *b* *c*

d *e*

Fig. 1. Images of typical structure of 96% *Cu*-3% *Si*-1% *Mn* bronze samples.
Samples 1 (*a*), **2** (*b*), **3** (*c*), **4** (*d*) and **5** (*e*)

Severe plastic deformation via multi-axial forging (Sample 3) and the associated microstructural changes resulted in a significant increase in both ultimate tensile strength (Fig. 2, *a*) and yield strength (Fig. 2, *b*) compared to the as-received hot-rolled and *WEBAM*-fabricated materials. This enhancement is a consequence of strain hardening according to the *Hall-Petch* relationship [14]. The UTS increased to 525 MPa and 519 MPa and the yield strength to 403 MPa and 298 MPa, while the relative elongation decreased from 70–100% to 18.1% (Fig. 2, *c*). Subsequent rolling (Sample 4) after forging further increased the *UTS* by 88 MPa and the yield strength by 376 MPa (Fig. 2, *a*, *b*), but reduced the relative elongation from 18.1% to 9.2%, compared with multi-axial forging (Fig. 2, *c*).

Low-temperature annealing (Sample 5) after rolling resulted in the highest strength values among all samples, with a *UTS* of 1022 MPa and a yield strength of 1,008 MPa (Fig. 2, *a*, *b*). Furthermore, this annealing improved the material's ductility, increasing the relative elongation from 8.2% to 12.2%.

Hardness represents a mechanical characteristic equally as important as strength and ductility (Fig. 2, *e*). The *WEBAM*-fabricated (Sample 1) and as-received hot-rolled (Sample 2) samples exhibit the lowest microhardness values of 0.86 GPa and 0.96 GPa, respectively (Fig. 2, *d*), which can be attributed to their coarse-grained microstructures [15, 16]. Severe plastic deformation via multi-axial forging (Sample 3) resulted in a threefold increase in microhardness compared to the coarse-grained Sample 1 and Sample 2. This enhancement stems primarily from grain refinement and the development of a high dislocation density. At the microstructural level, these changes produce strengthening through dislocation interactions and a substantial increase in dislocation density during deformation, directly reflected in the measured microhardness. A higher degree of deformation achieved through subsequent rolling (Sample 4) after multi-axial forging resulted in the maximum microhardness of 3.34 GPa among all investigated samples – 18% greater than after forging alone.

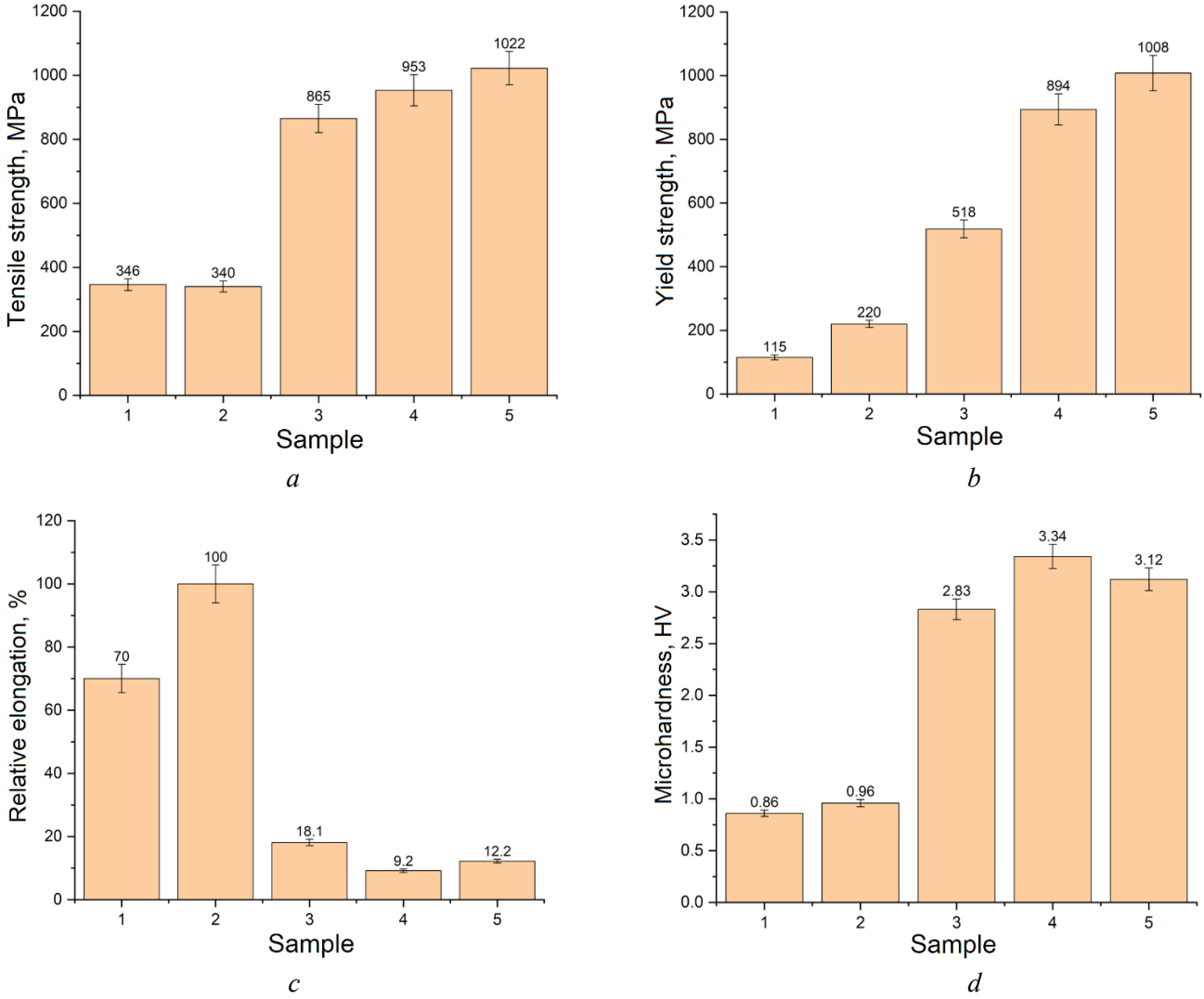

Fig. 2. Mechanical properties of 96% *Cu*-3% *Si*-1% *Mn* bronze samples

Low-temperature annealing (Sample 5) reduced the microhardness by approximately 7% relative to Sample 4, due to dislocation density reduction through recovery and polygonization processes.

During sliding friction, the coefficient of friction (*CoF*) undergoes significant evolution (Fig. 3, *a*). Initially, all bronze samples exhibited a high *CoF*, attributable to running-in processes within the steel-bronze tribological pair. During this initial stage, pre-existing oxide films are removed, forming a clean bronze surface. The interaction with this nascent surface results in significantly increased adhesion due to the enhanced molecular component of the friction force [17]. Subsequently, as the surface layer wears and sliding conditions evolve, the *CoF* may either increase or decrease, depending on the dominant wear mechanism and the specific characteristics of wear track formation.

The recorded friction coefficient data show that the *CoF* decreased over the first 15–25 minutes. For Sample 1 (*WEBAM*), this running-in stage transitioned into a period of steady-state sliding friction. The as-received hot-rolled sample (Sample 2) exhibited a sinusoidal *CoF* dynamic with a period of approximately 25 minutes, indicating a cyclical process of friction layer formation and degradation. A similar pattern was observed for the multi-axially forged sample (Sample 3), though with a longer period of about 30 minutes. Both Sample 2 and Sample 3 were characterized by a relatively monotonic increase and decrease in *CoF* within these intervals. In contrast, sliding for Sample 4 (forged + rolled) featured more frequent but lower amplitude *CoF* fluctuations, with a period of roughly 13 minutes. Sample 5 (forged + rolled + annealed) demonstrated oscillatory *CoF* behavior without a clearly defined periodicity.

The average *CoF* values, derived from the experimental data, are presented in Fig. 3, *b*. The results indicate that the highest average *CoF* is characteristic of the electron beam printed Sample 1. Sample 2

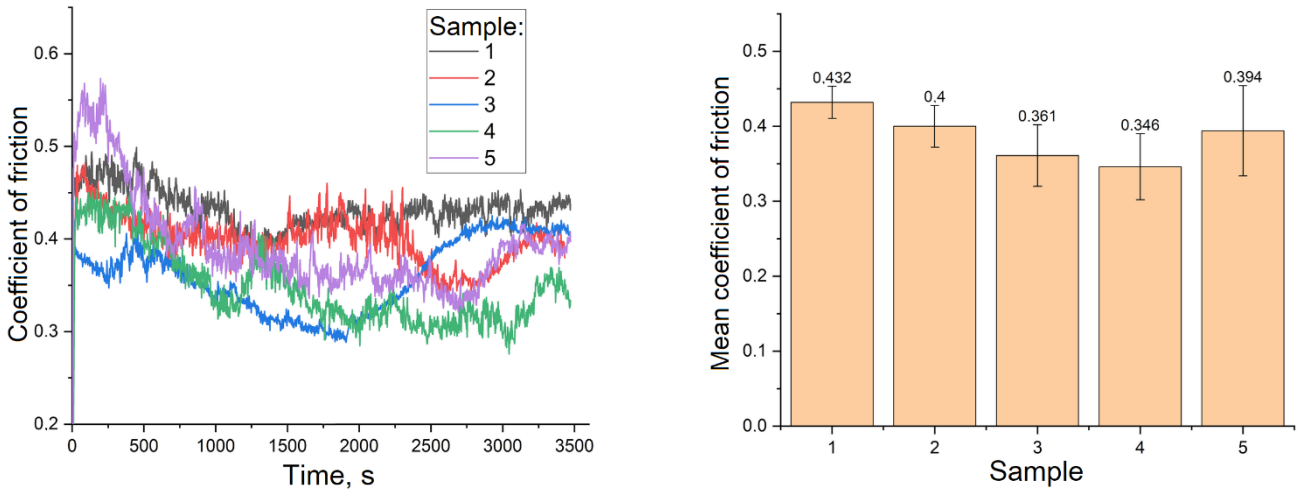

a *b*

Fig. 3. Coefficients of friction vs. time during sliding tests (*a*) and their average values (*b*)

(hot-rolled) and Sample 5 (forged + rolled + annealed) exhibited slightly lower values. Severe plastic deformation via multi-axial forging and subsequent rolling (Sample 3 and Sample 4) led to a significant reduction in the average *CoF* – by 9% to 25% – compared to the coarse-grained (Sample 1 and Sample 2) and heat-treated (Sample 5) conditions.

Vibration acceleration signals were recorded from two accelerometers during tribological tests. The accelerometers were mounted to record signals in the direction of normal pressure and friction forces, enabling detailed monitoring of the tribosystem's dynamic behavior.

During friction of the printed bronze (Sample 1), vibration accelerations in the normal (Fig. 4, *a*) and tangential (Fig. 4, *b*) directions reached values of ~4.4 m/s² and ~5.8 m/s², respectively. In the normal direction, vibrations occurred uniformly from the test onset, while fluctuations in the tangential direction showed no pronounced periodicity.

The as-received Sample 2 exhibited vibration accelerations of ~6.7 m/s² in the normal direction and ~9.7 m/s² in the tangential direction. In this case, significant fluctuations in acceleration amplitude were observed only in the tangential direction, substantially exceeding those recorded for other samples.

Sliding of bronze deformed by multi-axial forging (Sample 3) showed vibration accelerations of ~3.1 m/s² in the normal direction and ~3.6 m/s² in the tangential direction, with sufficiently uniform vibration acceleration amplitude and no significant fluctuations.

During friction of bronze deformed by rolling (Sample 4), vibration accelerations measured ~3 m/s² in the normal direction and ~3.2 m/s² in the tangential direction were the lowest levels among all samples investigated. Unlike other samples, amplitude fluctuations in the normal direction exceeded those in the tangential direction.

The heat-treated bronze Sample 5 displayed vibration acceleration amplitudes of ~3.5 m/s² in the normal direction and ~4.7 m/s² in the tangential direction. Annealing after severe plastic deformation by rolling resulted in increased vibration amplitude during sliding in both normal and tangential directions.

The difference in vibration acceleration amplitude between tangential and normal directions (D_v, Fig. 4, *c–e*) reflects changes in sliding friction conditions. Values closer to zero indicate more stable sliding friction. Higher tangential vibration amplitude suggests intense adhesive bonding (sticking) between the steel ball and bronze disk. When this bonding ruptures, the stick phase transitions to slip (stick-slip mode), causing sharp increases in tangential vibration acceleration. Normal direction vibrations likely result from wear particle formation and surface deterioration.

The data indicate that the most stable sliding occurs with Sample 4 (*SPD* by rolling) and Sample 3 (multi-axial forging). Conversely, Sample 1 (*WEBAM*) and Sample 2 (as-received) exhibit high-amplitude vibration accelerations during sliding with significant directional differences, suggesting strong adhesive

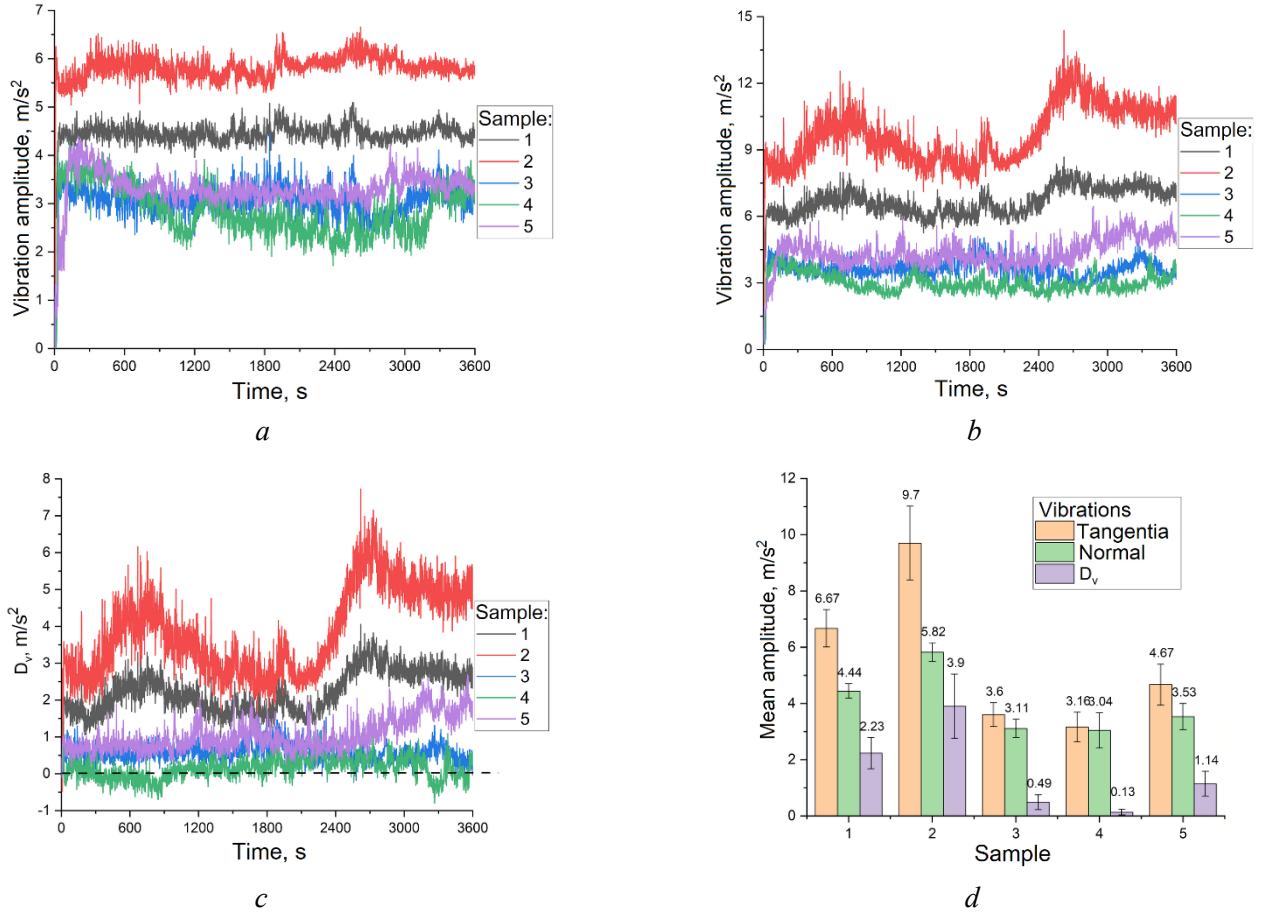

Fig. 4. Change in vibration acceleration amplitude during sliding friction in the normal (*a*) and tangential (*b*) directions, their difference (*c*), and average value (*d*)

interaction in the sliding pair. Low-temperature annealing (Sample 5) increased the D_v value, indicating enhanced adhesion during testing.

Previous studies [18] have established that the energy and median frequency (*MF*) of acoustic emission (*AE*) signals can characterize sliding friction modes. In this work, acoustic emission was detected and recorded using a sensor mounted on the sample during sliding friction. The *AE* signal waveforms were analyzed to determine the average values of energy (Fig. 5, *a*) and median frequency (Fig. 5, *b*).

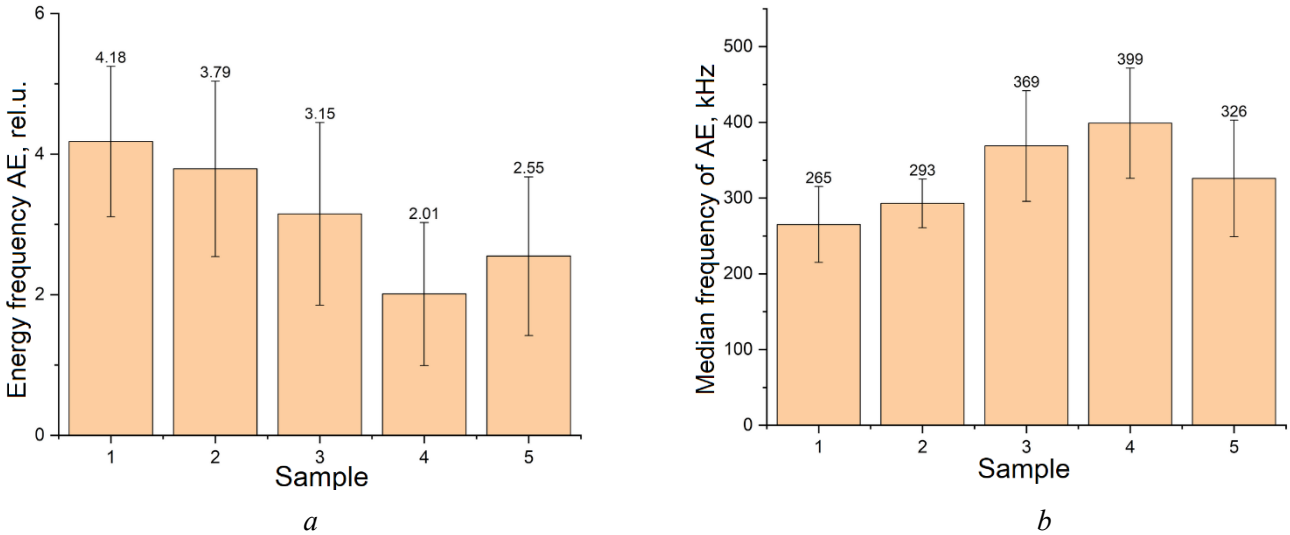

Fig. 5. Average energy (*a*) and median frequency (*b*) of acoustic emission (*AE*)

The results show a successive reduction in *AE* energy during sliding from coarse-grained Sample 1 to Sample 3, accompanied by a corresponding increase in *MF*. Sample 4 (rolled and heat-treated) exhibited the absolute minimum *AE* energy and maximum *MF*. Conversely, Sample 5 showed increased *AE* energy and reduced *MF* compared to Sample 4.

Comparison between vibrometry and acoustic emission data reveals a consistent pattern: *AE* energy increases in sliding modes characterized by high vibration acceleration amplitudes. This correlation occurs because significant stick-slip vibrations generate repeated impacts between contact asperities. The rupture of adhesive bonds and associated impacts excite powerful elastic waves in the material, consequently increasing *AE* energy. Conversely, these conditions reduce the median frequency, primarily due to adhesive bond rupture. Previous research [18] demonstrated that viscous crack formation in materials causes short-term *MF* drops. Additionally, changes in sliding friction conditions – such as wear particle formation, development of thick abrasion-resistant oxide layers, and surface layer deterioration – also affect the frequency characteristics of *AE* signals [19–21].

The current study confirms variations in friction and wear conditions across bronzes with different structural states, consistent with vibrometry data, friction coefficient measurements, and examination of worn surfaces.

Analysis of the wear track surfaces revealed characteristic wear features of silicon bronze in different structural states (Fig. 6). Sliding of Sample 1 produced a rough worn surface characterized by: light areas with relatively large wear grooves, smoother dark tribo-oxidized regions, and material displaced to the track periphery through plowing (Fig. 6, *a*). These features indicate the combined action of at least two wear mechanisms, specifically adhesive-oxidative wear.

The worn surface of the as-received Sample 2 (Fig. 6, *b*) exhibits curved wear grooves and plowing, with no oxidation traces, along with deformed material buildups resulting from adhesion-mediated transfer. In this process, plasticized bronze initially adheres to the steel counterface, then detaches and re-adheres to the disk's wear track surface. The absence of oxidation suggests a predominantly adhesive wear mechanism.

Sliding of Sample 3 (multi-axial forged) yields a wear track surface almost entirely covered by a uniform black layer of oxidized material (Fig. 6, *c*). The adhesive wear areas are small (250–500 μm) and contain oxide inclusions. The absence of plowing indicates insignificant plastic deformation of the material, which

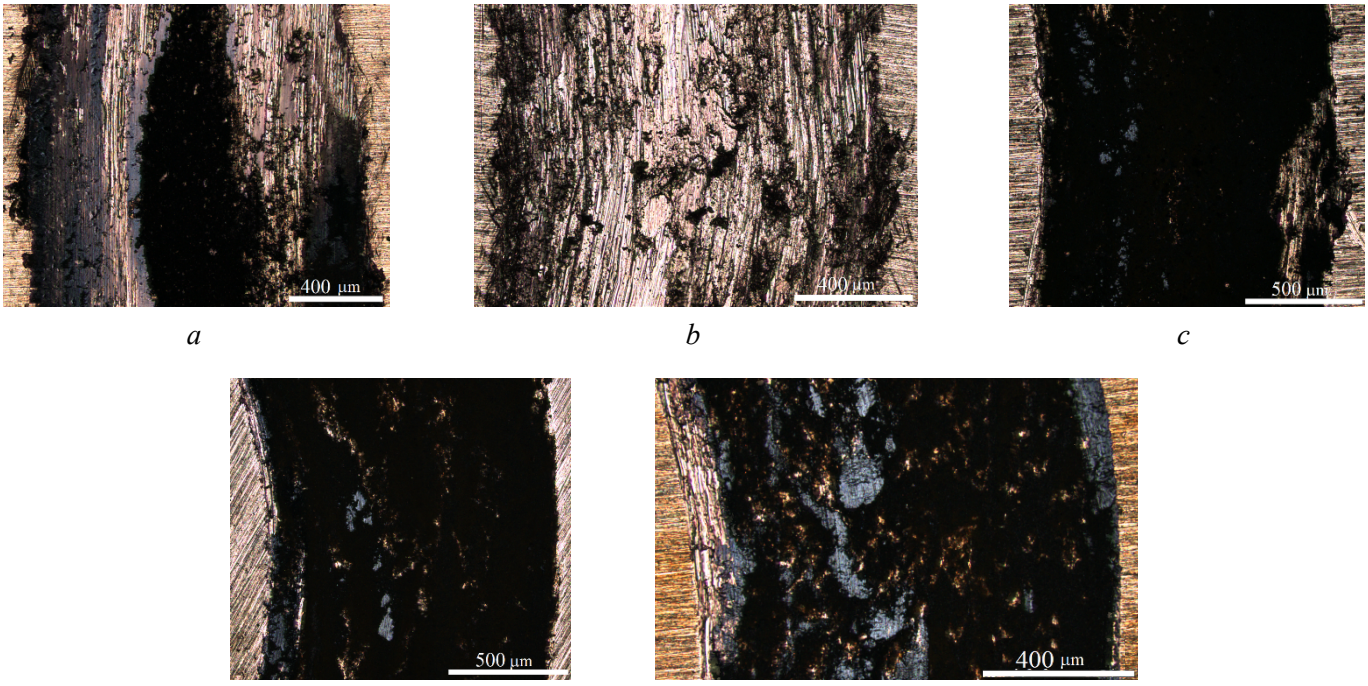

a *b* *c* *d* *e*

Fig. 6. Optical images of the wear track surfaces of 96% *Cu*-3% *Si*-1% *Mn* bronze samples. Samples 1 (*a*), 2 (*b*), 3 (*c*), 4 (*d*) and 5 (*e*)

is expected since Sample 3 underwent severe plastic deformation, acquiring higher hardness and lower ductility through work hardening.

The friction track surface of Sample 4 resembles that of Sample 3 (Fig. 6, *d*), indicating the predominance of oxidative wear. Apparently, from the sliding onset, an oxidized layer forms through adhesive transfer and compaction of wear particles. This layer exhibits resistance to mechanical impact and remains adherent to the bronze substrate, unlike more ductile samples that are susceptible to plastic deformation and cannot provide stable support for surface oxide layers.

Low-temperature annealing of Sample 5 after rolling resulted in the formation of slightly more extensive adhesive wear areas (Fig. 6, *e*) compared to Samples 3 and Samples 4. This phenomenon results from increased material plasticity and reduced load-bearing capacity, consequently enhancing adhesive wear components.

The worn surfaces of the ball bearing steel counterparts (balls) were examined to validate the findings obtained from the bronze samples (Fig. 7). The observed wear patterns confirm the previously identified differences in wear mechanisms across bronze structural states.

In cases of predominantly adhesive wear, a bronze transfer layer formed on the ball surface (Fig. 7, *b*). This layer consists of material transferred through adhesive wear from the ductile as-received bronze (Sample 2).

Under predominant oxidative wear, a black oxide layer formed on the ball surface (Fig. 7, *c*). These oxides accumulated in micro-depressions and represent detached surface layers from the work-hardened bronzes manufactured via multi-axial forging (Sample 3) and rolling (Sample 4).

Significant oxidation of the low-temperature annealed sample (Sample 5) resulted in oxide layer formation covering substantial portions of the wear track, which correspondingly contributed to oxide deposition on the ball surface.

Under mixed adhesive-oxidative wear conditions, cyclic formation and removal of the surface layer occurred within the wear track. Consequently, neither plastic bronze transfer nor stable oxide layers became established on the ball surface (Fig. 7, *a*).

The worn surfaces of the bronze samples were further characterized using scanning electron microscopy (*SEM*) equipped with energy-dispersive X-ray spectroscopy (*EDS*), as shown in Figs. 8 and 9. The backscattered electron (*BSE*) images in Figs. 8, *a–e* reveal the worn surfaces of all bronze samples, displaying distinct bright and dark regions. The *BSE* image contrast is governed by the local elemental composition, wherein elements with lower atomic numbers appear darker. Consequently, darker areas correspond to more heavily oxidized regions.

In this context, Sample 1 exhibits a worn surface with predominantly gray and bright areas, indicating limited oxidation (Fig. 8, *a*). The grayscale intensity further reveals that although oxides are present on the worn surface of the as-received Sample 2 (Fig. 8, *b*), they are confined to small, isolated areas of material adhered during the wear process. In contrast, Sample 3, Sample 4, and Sample 5 display extensively

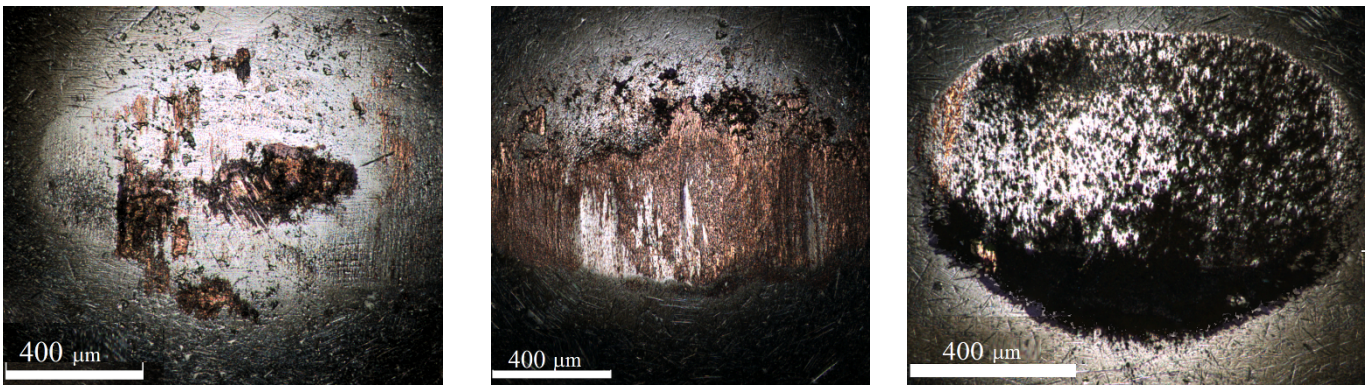

a *b* *c*

Fig. 7. Typical optical images of the ball surface after sliding against Sample 1 (*a*), Sample 2 (*b*), Samples 3–5 (*c*)

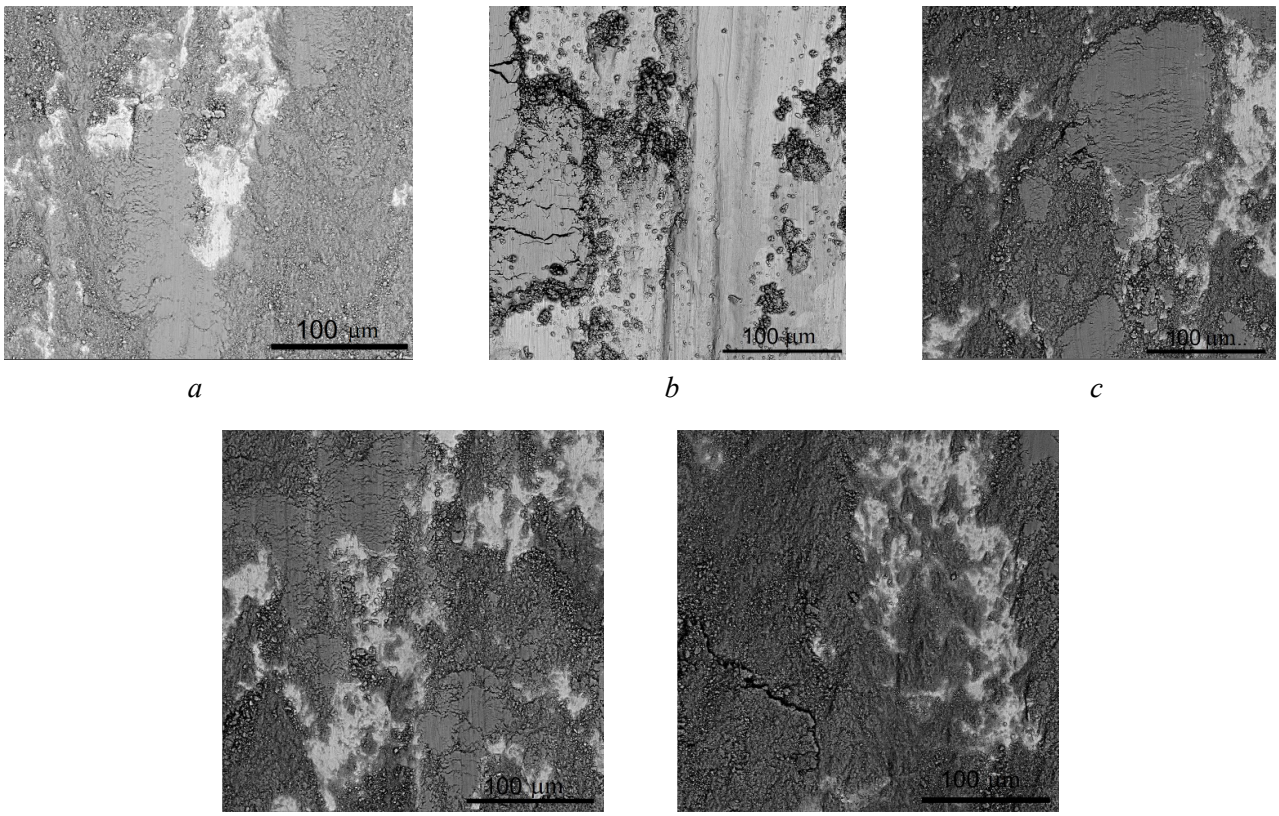

a *b* *c* *d* *e*

Fig. 8. SEM BSE images of the wear track surfaces of 96% *Cu*-3% *Si*-1% *Mn* bronze. Sample 1 (*a*), Sample 2 (*b*), Sample 3 (*c*), Sample 4 (*d*) and Sample 5 (*e*)

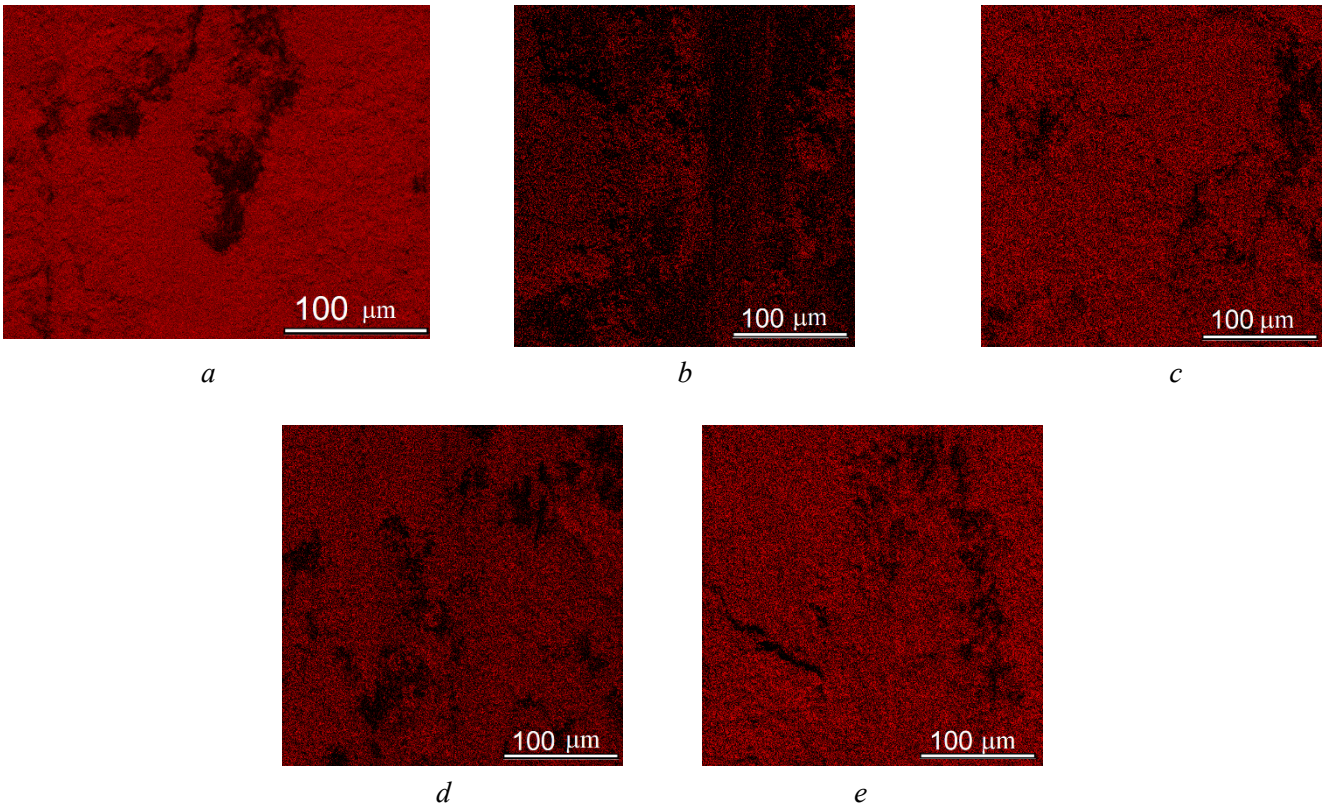

a *b* *c* *d* *e*

Fig. 9. EDS oxygen maps on the wear track surfaces of 96% *Cu*-3% *Si*-1% *Mn* bronze. Sample 1 (*a*), Sample 2 (*b*), Sample 3 (*c*), Sample 4 (*d*) and Sample 5 (*e*)

oxidized worn surfaces resulting from sliding on the severely plastically deformed (*SPD*) and strengthened materials (Figs. 8, *c–e*). The *EDS* elemental maps presented in Figs. 9, *a–e* confirm the presence of oxygen across these worn surfaces.

Fig. 10 presents the wear track profiles and corresponding cross-sectional area data. The obtained profiles (Fig. 10, *a*) reveal that sliding against Sample 1 and Sample 2 produced wear tracks with pronounced edge pile-ups. These pile-ups result from plastic deformation (ploughing) of the coarse-grained bronzes by the steel counter-body. In contrast, the *SPD*-strengthened Samples 3–5 exhibit no such pile-ups.

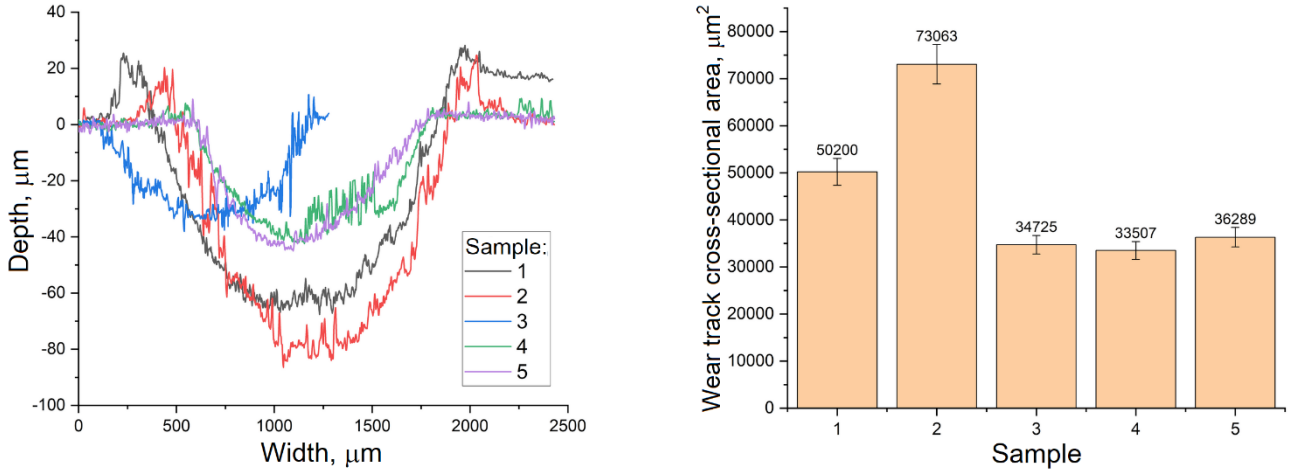

a *b*

Fig. 10. Cross-sectional profiles of wear tracks (*a*) of 96% *Cu*-3% *Si*-1% *Mn* bronze and their areas (*b*)

Measurements of the wear track cross-sectional areas (Fig. 10, *b*) indicate that the most severe wear occurred during sliding against Sample 2 (as-received condition). The wear volumes for Sample 1, Sample 3, and Sample 4 were lower than that of Sample 2 by factors of 1.6, 2.1, and 2.2, respectively. Wear was minimal during friction against the rolled bronze (Sample 4), being 2.2 times and 1.5 times lower than that of the hot-rolled and *WEBAM*-fabricated samples, respectively. The application of low-temperature annealing after rolling (Sample 5) increased wear by 10% compared to the condition obtained by rolling alone (Sample 4).

To analyze the effect of structural state on the subsurface deformation of silicon bronze induced by sliding friction, the regions beneath the worn surfaces were examined (Fig. 11). In coarse-grained Sample 1 and Sample 2 (Figs. 11, *a*, *b*), deformation bands are unevenly distributed across grains with different orientations relative to the loading axis. This is evidenced by developed systems of shear bands oriented at various angles to the sliding plane. The deformation zone extends to a depth of up to 50 μm below the worn surface in Sample 2, resulting from strong adhesive bonding within the friction pair. This adhesion causes the bronze material to stretch in the direction of the friction force, with the effect being most pronounced near the contact surface. Adhesive interaction is less intensive during sliding of Sample 2, consequently resulting in shallower plastic deformation penetration.

The *SPD*-processed samples (Figs. 11, *c–d*) consist of refined grains with high dislocation densities, making the identification of distinct deformation bands challenging. Instead, these samples exhibit curved shear bands and distorted grains. A thin tribological layer is visible immediately beneath the worn surfaces in these samples.

For quantitative assessment of subsurface deformation, the maximum penetration depth was measured. The results demonstrate that both the depth of plastic deformation penetration in the bronze (Fig. 12) and the wear behavior (Fig. 10) are governed by the material's mechanical characteristics (Fig. 2), which are in turn determined by its structural state.

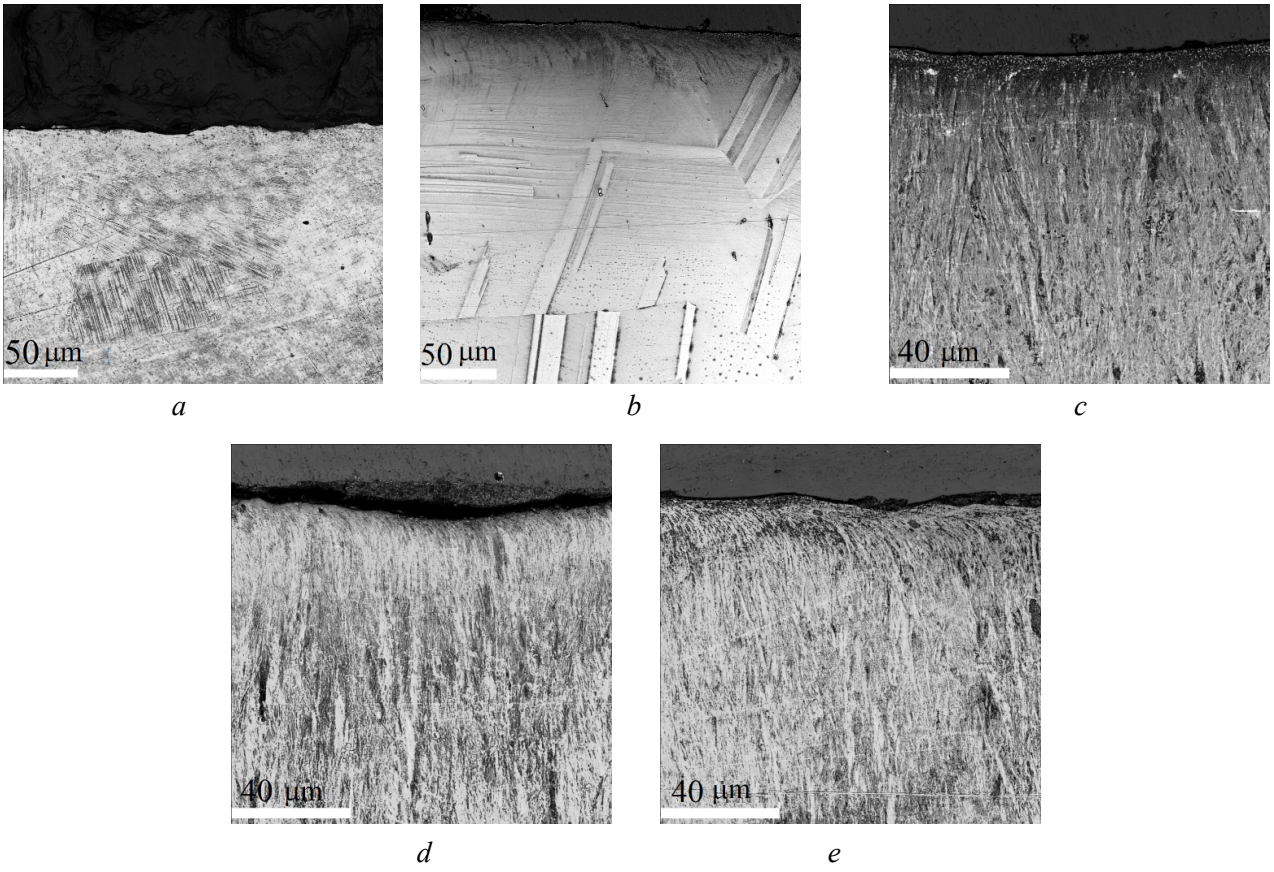

Fig. 11. Metallographic images of bronze 96% *Cu*-3% *Si*-1% *Mn* below the worn surfaces. Sample 1 (*a*), Sample 2 (*b*), Sample 3 (*c*), Sample 4 (*d*) and Sample 5 (*e*)

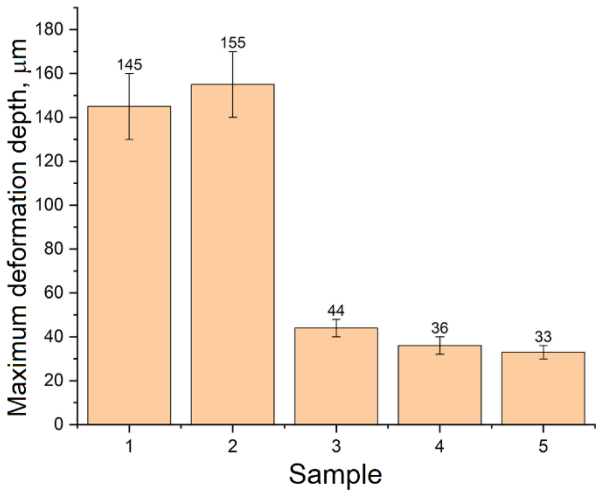

Fig. 12. Depth of penetration of plastic deformation below the worn surface

Conclusions

Experimental studies of the mechanical, tribological, and structural characteristics of a silicon bronze in different structural states – ranging from coarse-grained (produced by electron-beam additive manufacturing and hot rolling) to submicron-grained (resulting from severe plastic deformation via multi-axial forging and rolling) – yield the following conclusions:

1. The manufacturing method significantly influences the structural state of silicon bronze. Wire and electron-beam additive manufacturing (*WEBAM*) and hot rolling produce very large grains (150–600 μm

or more). Multi-axial forging produces nano-sized subgrains (lamellae under 100 nm) with high dislocation density. Subsequent rolling after forging further refines the structure, creating subgrains elongated along the rolling direction. Low-temperature annealing after rolling yields more equiaxed submicron grains (100–200 nm) with reduced dislocation density.

2. The structural state directly determines the mechanical properties. In the coarse-grained condition, the alloy exhibits low strength ($\sigma_u \approx 340$–346 MPa) and hardness (*HV* ≈ 0.86–0.96 GPa) but high ductility ($\delta \approx 70$–100%). The refined structures produced by *SPD* methods show a sharp increase in strength (σ_u up to 3 times higher) and hardness (*HV* up to 3.9 times higher), accompanied by a drop in ductility (δ decreasing from 100% to a minimum of 9.2%). Low-temperature annealing after rolling maintains high strength while slightly improving the ductility of the deformed material.

3. The structural state also governs the tribological characteristics. The lowest coefficient of friction was observed in samples subjected to severe plastic deformation. Furthermore, sliding friction for these samples was more stable, as evidenced by the lowest recorded amplitudes of vibration acceleration.

4. The structural state and mechanical properties significantly influence the wear mechanisms. The hot-rolled sample wears primarily by an adhesive mechanism. In high-strength samples processed by multi-axial forging and rolling, oxidative wear predominates. A mixed adhesive-oxidative mechanism was observed in the *WEBAM*-fabricated sample. The depth of plastic deformation penetration beneath the worn surface correlates strongly with the material's strength and hardness, reaching 145–155 μm in Sample 1 and Sample 2, but decreasing by a factor of 3.3–4.7 in the *SPD*-processed Samples 3–5.

5. Severe plastic deformation by multi-axial forging and rolling reduces the wear of silicon bronze by a factor of 2.1–2.2 compared to the as-received hot-rolled condition. Low-temperature annealing increases wear by 10% compared to the cold-worked Sample 4.

6. From a practical perspective, the results recommend the sequential application of multi-axial forging followed by rolling to achieve maximum wear resistance and sliding stability. This processing route yields high hardness (3.34 GPa), minimal wear (2.2 times lower than the hot-rolled condition), and the lowest and most stable coefficient of friction and vibration acceleration amplitude. Material with these properties is suitable for critical friction pairs operating under dry or boundary lubrication conditions where wear and vibration control are paramount.

7. To achieve maximum strength with acceptable ductility, low-temperature annealing after severe plastic deformation is recommended. This processing provides maximum strength with partial restoration of ductility. Material in this structural state is advisable for highly loaded structural components subjected to static and moderate dynamic loads, where strength is critical and wear resistance is of secondary importance.

References

1. Osintsev O.E., Fedorov V.N. *Med' i mednye splavy. Otechestvennye i zarubezhnye marki* [Copper and copper alloys. Domestic and foreign brands]. 2nd ed., rev. and enl. Moscow, Innovatsionnoe mashinostroenie Publ., 2016. 360 p. ISBN 978-5-9907638-3-8.

2. Kroupa A., Zobac O., Zemanova A., Richter K.W. CALPHAD-type reassessment of Cu-Si and full assessment of the Al-Cu-Si systems. *Journal of Phase Equilibria and Diffusion*, 2024, vol. 45, pp. 1206–1243. DOI: 10.1007/s11669-024-01160-5.

3. Shee S.K., Pal H., Pradhan S.K., De M. Correlation of microstructure with mechanical property of Cu-Si-Mn alloys. *Materials Engineering*, 1996, vol. 7 (4), pp. 431–442.

4. Nnakwo K.C., Mbah C.N., Daniel-Mkpume C.C. Investigation of the structural sensitive behavior of Cu-3Si-xMn ternary alloys. *Journal of King Saud University – Science*, 2019, vol. 31, pp. 1056–1063. DOI: 10.1016/j.jksus.2019.01.001.

5. Chromik R.R., Neils W.K., Cotts E.J. Thermodynamic and kinetic study of solid state reactions in the Cu–Si system. *Journal of Applied Physics*, 1999, vol. 86, pp. 4273–4281. DOI: 10.1063/1.371357.

6. Ezeobi U.E., Nwambu C.N., Nnuka E.E., Bosan B.M. Effect of solutionizing heat treatment on the structure and mechanical properties of silicon bronze (Cu-10wt%Si-2wt%Ni). *Archive of Biomedical Science and Engineering*, 2024, vol. 10, pp. 017–022. DOI: 10.17352/abse.000033.

7. Mattern N., Seyrich R., Wilde L., Baehtz C., Knapp M., Acker J. Phase formation of rapidly quenched Cu–Si alloys. *Journal of Alloys and Compounds*, 2007, vol. 429, pp. 211–215. DOI: 10.1016/j.jallcom.2006.04.046.

8. Kolubaev E.A., Rubtsov V.E., Chumaevsky A.V., Astafurova E.G. Micro-, meso- and macrostructural design of bulk metallic and polymetallic materials by wire-feed electron-beam additive manufacturing. *Physical Mesomechanics*, 2022, vol. 25 (6), pp. 479–491. DOI: 10.1134/S1029959922060017.

9. Kulczyk M., Skiba J., Przybysz S., Pachla W., Bazarnik P., Lewandowska M. High strength silicon bronze (C65500) obtained by hydrostatic extrusion. *Archives of Metallurgy and Materials*, 2012, vol. 57 (3), pp. 859–862. DOI: 10.2478/v10172-012-0094-4.

10. Tavolzhanskii S.A., Vedenkin E.D., Plisetskaya I.V., Nikitina A.A. Study of properties and structure of silicon bronze CuSi3Mn1 (C65500) wire at various stages of its production by continuous casting and subsequent drawing. *Metallurgist*, 2022, vol. 66, pp. 962–969. DOI: 10.1007/s11015-022-01408-w.

11. Filippov A., Shamarin N., Moskvichev E., Savchenko N., Kolubaev E., Khoroshko E., Tarasov S. The effect of heat input, annealing, and deformation treatment on structure and mechanical properties of electron beam additive manufactured (EBAM) silicon bronze. *Materials*, 2022, vol. 15, p. 3209. DOI: 10.3390/ma15093209.

12. Huang K., Logé R.E. A review of dynamic recrystallization phenomena in metallic materials. *Materials & Design*, 2016, vol. 111, pp. 548–574. DOI: 10.1016/j.matdes.2016.09.012.

13. Vorontsov A., Gurianov D., Zykova A., Nikonov S., Chumaevskii A., Kolubaev E. Phase formation and morphological characteristics of aluminum bronze and nickel alloy composites produced by the additive manufacturing process. *Scripta Materialia*, 2024, vol. 239, p. 115811. DOI: 10.1016/j.scriptamat.2023.115811.

14. Hansen N. Hall–Petch relation and boundary strengthening. *Scripta Materialia*, 2004, vol. 51, pp. 801–806. DOI: 10.1016/j.scriptamat.2004.06.002.

15. Yang B., Vehoff H. Dependence of nanohardness upon indentation size and grain size – A local examination of the interaction between dislocations and grain boundaries. *Acta Materialia*, 2007, vol. 55, pp. 849–856. DOI: 10.1016/j.actamat.2006.09.005.

16. Liu G., Ni S., Song M. Effect of indentation size and grain/sub-grain size on microhardness of high purity tungsten. *Transactions of Nonferrous Metals Society of China*, 2015, vol. 25, pp. 3240–3246. DOI: 10.1016/S1003-6326(15)63958-9.

17. Popov V.L., Heß M., Willert E. *Handbook of plane contact mechanics*. Berlin, Heidelberg, Springer, 2025. 260 p. DOI: 10.1007/978-3-662-70173-7.

18. Filippov A.V., Rubtsov V.E., Tarasov S.Yu. Acoustic emission study of surface deterioration in tribocontacting. *Applied Acoustics*, 2017, vol. 117, pp. 106–112. DOI: 10.1016/j.apacoust.2016.11.007.

19. Hase A., Sato Y., Shinohara K., Arai K. Identification of the wear process of a silver-plating layer by dual acoustic emission sensing. *Coatings*, 2021, vol. 11, p. 737. DOI: 10.3390/coatings11060737.

20. Morita M., Tachiyama S., Onodera K., Hase A. Study on reaction mechanism of sulfur and phosphorus type additives using an acoustic emission technique. *Tribology Online*, 2022, vol. 17, pp. 78–85. DOI: 10.2474/trol.17.7.

21. Mishina H., Hase A. Effect of the adhesion force on the equation of adhesive wear and the generation process of wear elements in adhesive wear of metals. *Wear*, 2019, vol. 432–433, p. 202936. DOI: 10.1016/j.wear.2019.202936.

Conflicts of Interest

The authors declare no conflict of interest.